

**Fractally Fourier decimated homogeneous turbulent shear flow in noninteger dimensions**

Mani Fathali\* and Saber Khoei

*Department of Aerospace Engineering, K.N. Toosi University of Technology, Tehran, Iran*

(Received 16 November 2016; published 24 February 2017)

Time evolution of the fully resolved incompressible homogeneous turbulent shear flow in noninteger Fourier dimensions is numerically investigated. The Fourier dimension of the flow field is extended from the integer value 3 to the noninteger values by projecting the Navier-Stokes equation on the fractal set of the active Fourier modes with dimensions  $2.7 \leq d \leq 3.0$ . The results of this study revealed that the dynamics of both large and small scale structures are nontrivially influenced by changing the Fourier dimension  $d$ . While both turbulent production and dissipation are significantly hampered as  $d$  decreases, the evolution of their ratio is almost independent of the Fourier dimension. The mechanism of the energy distribution among different spatial directions is also impeded by decreasing  $d$ . Due to this deficient energy distribution, turbulent field shows a higher level of the large-scale anisotropy in lower Fourier dimensions. In addition, the persistence of the vortex stretching mechanism and the forward spectral energy transfer, which are three-dimensional turbulence characteristics, are examined at changing  $d$ , from the standard case  $d = 3.0$  to the strongly decimated flow field for  $d = 2.7$ . As the Fourier dimension decreases, these forward energy transfer mechanisms are strongly suppressed, which in turn reduces both the small-scale intermittency and the deviation from Gaussianity. Besides the energy exchange intensity, the variations of  $d$  considerably modify the relative weights of local to nonlocal triadic interactions. It is found that the contribution of the nonlocal triads to the total turbulent kinetic energy exchange increases as the Fourier dimension increases.

DOI: [10.1103/PhysRevE.95.023115](https://doi.org/10.1103/PhysRevE.95.023115)**I. INTRODUCTION**

As an overall description, hydrodynamic turbulence is a spatiotemporal chaotic flow field evolution, involving interactions among an extremely wide range of scales. Due to this chaotic nature, the turbulence dynamics can show acute sensitivity to the variations of the specifying flow field parameters [1]. Although the kinematical quantities such as the turbulent intensity and the integral length scale at the initial or upstream flow field are mainly considered as the specifying parameters, it has been observed that the turbulence dynamics can also be strongly influenced by the variation of the number of the spatial dimensions.

More specifically, the two-dimensional turbulence can show qualitatively and quantitatively different dynamics compared to its three-dimensional turbulence counterpart [2]. Indeed, by reducing the physical space dimension from the relevant value 3 to 2, the direction of the energy cascade is reversed towards the infrared (large-scale) region of the spectrum. Moreover, the three-dimensional turbulence shows pronounced small-scale intermittency and anomalous scaling while the statistics of the small-scale structures in the two-dimensional turbulence demonstrates some signatures of the Gaussianity and self-similar behavior.

These profoundly different characteristics of the turbulence in two- and three-dimensional flow fields have founded a viable framework for investigating the transitional behavior of turbulence in  $2 \leq d \leq 3$  dimensions. This feature of the space dimensionality, as a controlling parameter, mainly originates from the statistical physics problems. Indeed, in many-body problems, dimension plays an essential role in characterizing

the strength of the interactions among many degrees of freedom [3,4].

Notably, despite the enormous number of researches done on the two-dimensional turbulence (see among others Refs. [5–10]), a few researches have been carried out to investigate the impact of the variation of the dimension on the turbulence dynamics.

In one of the earliest studies, Nelkin [11] theoretically investigated the existence of the crossover dimension for validity of Kolmogorov's scaling law. Using dynamical reasoning, he showed that for  $2 < d < 8/3$ , the Kolmogorov scaling law in the limit of infinite Reynolds number is exact, and at  $d = 3.0$  a small correction has to be added.

By introducing the dimension as a formal parameter into the renormalization method, Forster *et al.* [12] proposed a systematic method for calculating stationary, fully developed  $d$ -dimensional turbulence with a high Reynolds number, for arbitrary noninteger  $d$ . Using this methodology, Fournier and Frisch [13] examined the transitional behavior of the turbulence evolution for dimensions at  $2 \leq d \leq 3$ . By probing the power-law behavior of the infrared and ultraviolet regions of the energy spectrum, they found a crossover dimension  $d \approx 2.03$  for the transition between the two- and three-dimensional characteristics of the energy cascade, i.e., backward and forward energy transfer.

In a later study, L'vov *et al.* [14] investigated the transitional behavior of the turbulence with dimension lower than 2. Using analytical reasoning, they obtained the crossover dimension  $d = 4/3$  for the validity of Kolmogorov's scaling law, in which the enstrophy flux is identically zero and the statistical properties of the small-scale structures are exactly Gaussian. Moreover, based on their findings, within  $4/3 \leq d \leq 2$  the enstrophy flux remains negligibly small and the small-scale statistics show insignificant deviation from Gaussianity.

\*mfathali@kntu.ac.ir

In a different approach, Giuliani *et al.* [15] investigated the transitional behavior of the Gledzer-Ohkitani-Yamada (GOY) shell model from  $d = 2.0$  to  $d = 3.0$ . To change the effective dimension of the shell model, the helicity conservation (three-dimensional invariant) is continuously varied to an enstrophy conservation (two-dimensional invariant). Based on their calculations, a crossover dimension for the GOY shell model is obtained, in which the energy distribution among infrared shells develops into an equipartition state while the statistical properties show deviation from the Gaussianity.

Using direct numerical simulation (DNS), Celani *et al.* [16] investigated the transition of the isotropic turbulence evolution between two and three dimensions. To resemble the transition from a three-dimensional isotropic system to the two-dimensional one, the aspect ratio of the computational domain is continuously reduced. Above the crossover aspect ratio 1:2, they observed a linear growth in the kinetic energy, which indicates the energy transfer toward large scales through an inverse energy cascade, as in two-dimensional flows.

In the same line as the L’vov’s research, Frisch *et al.* [17] examined the flow field evolution of the high Reynolds number isotropic turbulence in dimensions at  $1.5 \leq d \leq 2$ . To this end, they reduced the degrees of freedom of the Navier-Stokes equation in the Fourier space, using a generalized Galerkin projection. Therefore, without changing the spatial dimension and the corresponding dynamical invariants of the Navier-Stokes equation, turbulent flow field evolution poses a Fourier fractal dimension  $d$ . Performing different DNSs, they demonstrated that the inverse energy cascade, as a key feature of the two-dimensional turbulence, persists in dimensions lower than 2. Moreover, they observed that lowering the Fourier fractal dimension leads to the reduction of this backward spectral energy transfer, while resulting in a monotonic increase in the Kolmogorov constant of the energy spectrum.

Based on the same fractal decimation method proposed by Frisch *et al.* [17], in a more recent research Lanotte *et al.* [18] examined the evolution of a high Reynolds number isotropic turbulence with Fourier fractal dimensions  $d \in \{2.5, 2.8, 2.9, 2.99, 2.999, 3\}$ . Their DNS results revealed that the main characteristic of the three-dimensional turbulence, i.e., the direct energy cascade, persists in this range of dimensions. Further, they reported that by reducing  $d$ , the small-scale intermittency reduces quickly. Using scaling relations, they also showed that the inertial range power law of the energy spectrum is directly influenced by the variation of the Fourier dimension.

In a latter study, Lanotte *et al.* [19] investigated the impact of the fractal Fourier decimation on the vortex dynamics in terms of the statistics of the velocity and the velocity gradient tensor. They observed that the reduction of the Fourier dimension strongly hampers the vortex stretching process and increases the flow field Gaussianity.

In view of the above-mentioned studies, the impact of the Fourier dimension reduction on several important features of turbulence has been examined. However, there are many fundamental questions, which have not been addressed yet. The spectral energy transfer is perhaps one of the most fundamental dynamical mechanisms of turbulence, which shows nontrivial

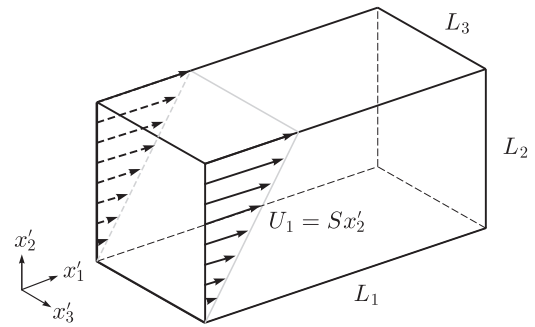


FIG. 1. Schematic representation of homogeneous turbulent shear flow (HTSF) configuration, with  $U_1$  as the mean velocity,  $S$  the imposed uniform mean shear, and  $(L_1, L_2, L_3)$  representing the domain size.

differences in two and three dimensions. However, it is not clear how the variation of the Fourier dimension modifies the triadic nonlinear energy transfer mechanism.

Besides these issues, there are other turbulence features, such as the influence of the reduction of the Fourier dimension on the large and small-scale anisotropy, which the impact of dimensionality on them cannot be investigated in the framework of an isotropic turbulence.

This study is motivated by the above-mentioned questions. More specifically, the objective of this research is to address the impact of the variation of the Fourier fractal dimension on (1) the overall flow field evolution, (2) the infrared and ultraviolet regions of the spectrum based on the small and large scales dynamics, and (3) the nature of the spectral energy transfer mechanisms.

To this end, the flow field evolution of the homogeneous turbulent shear flow (HTSF) at different Fourier fractal dimensions  $2.7 \leq d \leq 3.0$  is investigated, using DNS. The Fourier fractal dimension of the flow field is varied by projecting the turbulent flow field evolution on a reduced set of the Fourier modes, known as the fractal decimation method [17,18].

The HTSF is an unbounded homogeneous turbulence, which is subjected to a uniform mean velocity gradient in one spatial direction (see Fig. 1). This flow field configuration can provide an appropriate framework for extending the line of researches mentioned above. Despite its simplicity, this flow field configuration contains complex turbulent features, such as the large-scale anisotropy, kinetic energy production, and hairpin vortical structures quite similar to those observed in a wall-bounded turbulence (see among others Refs. [20–24]).

The remainder of the paper is organized as follows. In Sec. II, the flow field configuration is briefly explained along with the governing equations and variation of the flow field Fourier dimension. In Sec. III, the numerical method and the simulation specifications are presented. The results are gathered in Sec. IV. First, the overall flow field evolution is discussed in Sec. IV A. Next, dynamics of the large and small scales turbulence are investigated in Secs. IV B and IV C. The last part of the results, i.e., Sec. IV D, is devoted to the spectral energy transfer mechanisms. Finally, some conclusions are summarized in Sec. V.

## II. FLOW FIELD DESCRIPTION AND GOVERNING EQUATIONS

The Navier-Stokes (NS) equation for the evolution of an incompressible flow can be written as

$$\begin{aligned} \frac{\partial \tilde{u}_i}{\partial x'_i} &= 0, \\ \frac{\partial \tilde{u}_i}{\partial t'} + \frac{\partial(\tilde{u}_i \tilde{u}_j)}{\partial x'_j} &= -\frac{\partial \tilde{p}}{\partial x'_i} + \nu \frac{\partial^2 \tilde{u}_i}{\partial x'_j \partial x'_j}, \end{aligned} \quad (1)$$

where  $x'_i$ ,  $t'$ ,  $\tilde{u}_i$ , and  $\nu$  denote the  $i$ th spatial coordinate, time,  $i$ th velocity component, and the fluid kinematic viscosity. In the above equations, the constant density is absorbed into the static pressure, resulting in the modified pressure  $\tilde{p}$ . Using Reynolds decomposition, the dependent variables  $\tilde{u}_i = U_i + u_i$  and  $\tilde{p} = P + p$  can be decomposed into the mean and the fluctuating parts, denoted by the upper-case and the lower-case letters, respectively. Introducing this decomposition into the NS equation (1), the governing equations for the mean and fluctuating fields can be obtained [25].

For the considered HTSF in this research, the mean pressure  $P$  is uniform in space and constant in time. The mean flow is denoted by  $\mathbf{U} = (Sx'_2, 0, 0)$ , where the shear rate  $S$ , similar to the mean pressure, is uniform in space and constant in time.

Such a mean flow preserves the homogeneity of an initially homogeneous turbulence during the flow field evolution. On the other hand, a homogeneous turbulence cannot influence the evolution of its carrier mean flow (Ref. [26], p. 112). Here, it can be easily checked that the considered mean flow is a steady state solution of the NS equation and, therefore, the turbulence flow field evolution can be inclusively described by the governing equation of the fluctuating part:

$$\begin{aligned} \frac{\partial u_i}{\partial x'_i} &= 0, \\ \frac{\partial u_i}{\partial t'} + \frac{\partial(u_i u_j)}{\partial x'_j} + Sx'_2 \frac{\partial u_i}{\partial x'_1} + S\delta_{i1} u_2 &= -\frac{\partial p}{\partial x'_i} + \nu \frac{\partial^2 u_i}{\partial x'_j \partial x'_j}, \end{aligned} \quad (2)$$

where  $\delta_{i1}$  is the Kronecker  $\delta$ . Despite the homogeneity of the turbulent field, the second equation (2) is not periodic in the laboratory frame, due to the explicit dependence of the convective term, i.e.,  $Sx'_2$ , on the normal direction. This nonperiodic term can be eliminated by considering the flow field evolution in a reference frame, which deforms with the mean flow [27]:

$$x_i = x'_i - (St)x'_2 \delta_{i1} \quad \text{and} \quad t = t', \quad (3)$$

where  $t$  and  $x_i$  represent transformed moving coordinates. Using the chain rule, the transformed equations into the moving frame can be written as follows:

$$\begin{aligned} \frac{\partial u_i}{\partial x_i} - St \frac{\partial u_2}{\partial x_1} &= 0, \\ \frac{\partial u_i}{\partial t} + \frac{\partial(u_i u_j)}{\partial x_j} - St u_2 \frac{\partial u_i}{\partial x_1} + Su_2 \delta_{i1} &= -\frac{\partial p}{\partial x_i} + \nu \frac{\partial^2 u_i}{\partial x_j \partial x_j}, \end{aligned}$$

$$\begin{aligned} &= -\left( \frac{\partial p}{\partial x_i} - St \frac{\partial p}{\partial x_1} \delta_{i2} \right) \\ &+ \nu \left( \frac{\partial^2 u_i}{\partial x_j \partial x_j} - 2St \frac{\partial^2 u_i}{\partial x_1 \partial x_3} + 2S^2 t^2 \frac{\partial^2 u_i}{\partial x_1 \partial x_1} \right). \end{aligned} \quad (4)$$

Since the periodic boundary conditions can be applied to Eqs. (4), any flow field variable  $\phi(\mathbf{x}, t)$  can be expanded by Fourier coefficients  $\hat{\phi}(\mathbf{k}, t)$  [28],

$$\phi(\mathbf{x}, t) = (\delta k)^3 \sum_{\mathbf{k}} \hat{\phi}(\mathbf{k}, t) \exp(i\mathbf{k} \cdot \mathbf{x}), \quad (5)$$

$$\hat{\phi}(\mathbf{k}, t) = (2\pi)^{-3} \int \phi(\mathbf{x}, t) \exp(-i\mathbf{k} \cdot \mathbf{x}) d\mathbf{x},$$

where  $\delta k \equiv 2\pi(L_1 L_2 L_3)^{-1/3}$ , and  $i \equiv \sqrt{-1}$ . Moreover, the wave vector  $\mathbf{k}$  is given by

$$\mathbf{k} = 2\pi(n_1/L_1, n_2/L_2, n_3/L_3), \quad (6)$$

where  $n_i$  are integers, each of which varies over the range from  $-N_i/2$  to  $N_i/2 - 1$  and  $N_i$  is the number of the expansion terms (grid points) in the  $x_i$  direction. Application of the Fourier transform (5) to equations (4) results in

$$\begin{aligned} k_i \hat{u}_i &= 0, \\ \left( \frac{d}{dt} + \nu k^2 \right) \hat{u}_i &= \left( -\delta_{ij} + \frac{k_i k_j}{k^2} \right) \mathcal{F}\{u_i u_j\} \\ &+ 2 \frac{k_i k_1}{k^2} S \hat{u}_2 - \delta_{i1} S \hat{u}_2. \end{aligned} \quad (7)$$

Here  $k^2 = k_i k_i$  is the wave vector module,  $\hat{u}_i(\mathbf{k}, t)$  is the Fourier coefficient of the fluctuating velocity field, and  $\mathcal{F}\{u_i u_j\}$  represents the Fourier transform of the nonlinear quadratic terms  $u_i u_j$ . Moreover, wave vectors in the moving and laboratory references, i.e.,  $k_i$  and  $k'_i$ , are related as follows:

$$k_i = k'_i - St k'_1 \delta_{i2}. \quad (8)$$

Using the fractal decimation procedure in Fourier space, introduced by Frisch *et al.* [17], it is possible to continuously reduce the Fourier dimension of the governing equation (7) to the noninteger values below 3, i.e.,  $d \leq 3$ . Concisely, in the fractal decimation procedure, the governing equation, as well as its initial condition, are projected on a pre-selected set of the Fourier modes as follows:

$$\frac{\partial v_i}{\partial t} = P^D \{ \mathcal{N} \mathcal{L}(v_i, v_j) \} + \mathcal{L}(v_i), \quad (9)$$

where  $v_i(\mathbf{x}, t)$  is the decimated incompressible field, and  $\mathcal{N} \mathcal{L}$  and  $\mathcal{L}$  denote the corresponding nonlinear and linear terms of the NS equation, respectively. The decimated field  $v_i(\mathbf{x}, t)$  is defined based on the following projection in Fourier space:

$$v_i(\mathbf{x}, t) = P^D \{ u_i(\mathbf{x}, t) \} = (\delta k)^3 \sum_{\mathbf{k}} \alpha(\mathbf{k}) \hat{u}_i(\mathbf{k}, t) \exp(i\mathbf{k} \cdot \mathbf{x}), \quad (10)$$

where  $\alpha(\mathbf{k})$  are independent, prespecified, time-frozen random coefficients:

$$\alpha(\mathbf{k}) = \begin{cases} 1, & \text{with probability } h_k, \\ 0, & \text{with probability } 1 - h_k. \end{cases} \quad (11)$$

To ensure the reality of the decimated velocity field  $v_i(\mathbf{x}, t)$ , coefficients  $\alpha(\mathbf{k})$  are constrained with Hermitian symmetry  $\alpha(\mathbf{k}) = \alpha(-\mathbf{k})$ . The key element of this method is the probability function  $h_k$ , which is considered as

$$h_k = k^{d-3}, \quad 0 < d \leq 3. \quad (12)$$

This probability function ensures that the number of the active Fourier modes within the sphere with spectral radius  $k$  grows as  $k^d$ . Therefore, although the decimated field evolves in a three dimensional space,  $v_i(\mathbf{x}, t)$  effectively possesses a number of Fourier modes which correspond to a turbulence flow field evolution in a  $d$ -dimensional Fourier space.

Accordingly, the projection (10) reformulates the problem on a fractal set corresponding to the Fourier dimension  $d$ , without breaking the statistical homogeneity and the Galilean invariance. Due to the preservation of the homogeneity, similar to the original NS equation in the integer dimension  $d = 3.0$ , the evolution of the decimated HTSF can also be inclusively described by the governing equations of the decimated fluctuating field. Moreover, validation of the Galilean invariance allows transforming the fluctuating field into the moving frame, using Rogallo's transformation (3).

Therefore, the solution procedures for calculating the HTSF field in the fractal and integer Fourier dimensions are completely similar. However, it should be noted that to preserve the idempotency of the projection (10), which ensures the inviscid conservation of the quadratic quantities, the set of the active Fourier modes has to be preselected from the wave vectors in the moving reference.

### III. METHOD OF SOLUTION

In this section the numerical method and the simulation setup are briefly discussed.

#### A. Numerical algorithm

The governing equation (7) is numerically solved using the Fourier pseudospectral method with triply periodic boundary conditions. The nonlinear convection terms are treated based on the 3/2 de-aliasing rule. The solution is advanced in time using a second-order Runge-Kutta method.

As a result of the coordinate transformation (8), the wave vector  $k_2$  is explicitly related to  $St$ , where  $S$  and  $t$  are the shear rate and time, respectively. This time dependency poses two issues, which have to be considered in the solution procedure. The first issue is related to the incompressibility condition. Starting from an incompressible field at time step  $t_n$ , the projection tensor  $(\delta_{ij} - k_i k_j / k^2)$  in the momentum equation (7) enforces the continuity condition with respect to the wave vector  $k_i(t_n)$ . Since the wave vector  $k_i$  rotates during the time interval  $[t_n, t_{n+1}]$ , the obtained Fourier mode  $\hat{u}_i(k_i, t_{n+1})$  does not satisfy the incompressibility condition with respect to  $k_i(t_{n+1})$ . To prevent deviation from the incompressibility condition, the right hand side of the momentum equation (7) has to be projected onto the perpendicular plane of the wave vector  $k(t_{n+1})$ , before updating the Fourier modes at each Runge-Kutta stage.

The second issue is related to the growth of the wave vector  $k_2$ . During the flow field evolution, the wave vector  $k_2 = k'_2 -$

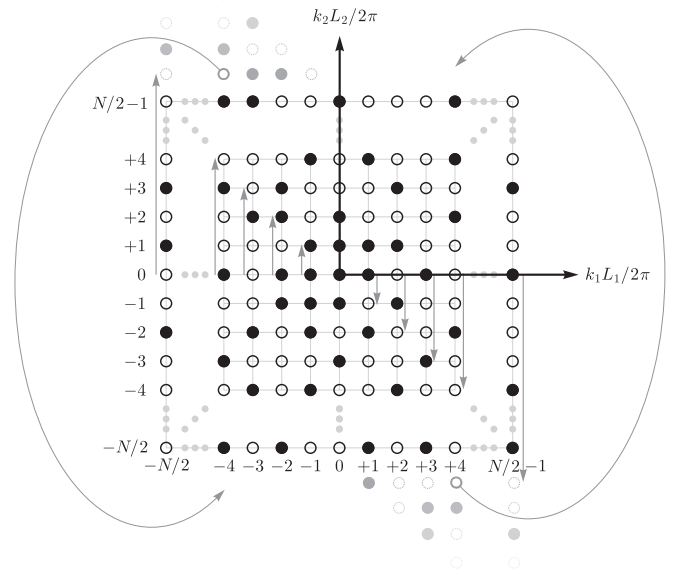


FIG. 2. Schematic representation of the remeshing procedure in the  $(k_1, k_2)$  plane. The straight arrows inside the lattice represent the shifts of the Fourier modes after each remeshing according to relabelling (13). The magnitudes of these arrows are proportional to the magnitude of the shift for each column. The circles in black (white) are active (decimated) Fourier modes. The grey circles outside the lattice indicate the exited active (decimated) Fourier modes, which are re-entered as the active (decimated) modes from the opposite boundary, as indicated with big arrows around the lattice.

$Stk'_1$  and the corresponding terms in Eq. (7) can unboundedly grow. Therefore, to avoid subsequent numerical errors, the variation of  $k_2$  has to be limited within a prespecified interval, which is performed through a remeshing procedure [27].

To this end, at specific times  $St = (n + 1/2)(L_1/L_2), n = \{0, 1, 2, \dots\}$ , the wave vector  $k'_2$  is periodically relabelled as

$$k'_2 \rightarrow k'_2 + k'_1 \left( \frac{L_1}{L_2} \right), \quad (13)$$

while  $k'_1$  and  $k'_3$  remain unchanged [29]. This relabelling ensures the boundedness of the wave vector  $\mathbf{k}$ .

The remeshing procedure also shifts the Fourier modes in the wave space according to relabelling (13). Therefore, after each remeshing, some Fourier modes exit the spectral domain from one of the boundaries in the  $k_2$  direction. To accomplish the aliasing-free remeshing procedure, any Fourier mode that exits the spectral domain from one boundary is re-entered from the opposite boundary with zero amplitude.

In evolution of the fractally decimated HTSF, to preserve the number of the active Fourier modes during the remeshing procedure, the exited active (decimated) Fourier modes are re-entered as the active (decimated) modes from the opposite boundary. Figure 2 schematically demonstrates the movement and the recycling of the Fourier modes during the remeshing procedure.

It should be noted that although the number of the active and decimated Fourier modes does not change, the skeleton of the fractal Fourier set, and consequently its fractal dimension, inevitably changes during the remeshing procedure. However,

TABLE I. The specification of the computational setup and the initial velocity field used for all simulations (in mks units).

Dimension of the fractal set of the active Fourier modes ( $d$ )	3, 2.9, 2.8, 2.7
Resolution ( $N_1 \times N_2 \times N_3$ )	$512^3$
Domain size ( $L_1 \times L_2 \times L_3$ )	$4\pi \times 2\pi \times 2\pi$
Uniform mean shear rate ( $S$ )	16
Kinematic viscosity ( $\nu$ )	0.01
Integral length scale [ $\mathcal{L}$ Eq. (15)]	0.33
Taylor microscale ( $\lambda^2 \equiv u_i^2 / (\partial u_i / \partial x_i)^2$ )	0.26
Dissipation rate ( $\epsilon$ )	2.918
Turbulent kinetic energy ( $q_0^2 \equiv \overline{u_i u_i}$ )	1.8471
Constant spectrum coefficient [ $E_0$ in Eq. (14)]	$1.1244 \times 10^{-3}$
Spectrum peak energy wave number [ $k_0$ in Eq. (14)]	8
Nondimensional shear parameter ( $S^* \equiv Sq^2/\epsilon$ )	10.13
Reynolds number based on the Taylor microscale ( $Re_\lambda \equiv q^2\lambda/\nu$ )	35
Reynolds number based on the integral length scale ( $Re_\mathcal{L} = q^2\mathcal{L}/\nu$ )	46

it is found that for the considered range of the relevant simulation parameters, i.e., the fractal Fourier dimension  $d$  and the resolution, the variation of the skeleton of the decimated Fourier set does not affect the averaged fractal dimension by more than 1% and has negligible effects on the evolution of the decimated flow (see the Appendix).

### B. Simulation specifications

In this research, four DNSs have been carried out at different values of Fourier dimensions  $d = 3.0, 2.9, 2.8,$  and  $2.7$ . The computational domain is a rectangular box with size  $4\pi \times 2\pi \times 2\pi$ , discretized using  $512^3$  grid points. The lower bound of the fractal dimension, i.e.,  $d = 2.7$ , is set based on the resolution considerations. Indeed, the required resolution to obtain the reliable statistics significantly increases as the dimension  $d$  decreases.

All simulations are initialized with a stochastic solenoidal isotropic velocity field with the prescribed energy spectrum

$$E(k) = E_0 k^4 \exp(-2k^2/k_0^2). \quad (14)$$

Here,  $k_0$  defines the location of the peak in the energy spectrum and the constant  $E_0$  is closely related to the initial turbulent kinetic energy. For all simulations, the mean flow shear is  $S = 16$  and the initial Reynolds number based on the Taylor microscale is  $Re_\lambda = 35$ . The detailed specification of the

computational domain and the initial velocity field used for all simulations are listed in Table I.

Figure 3 demonstrates the quality of the simulations by presenting time evolutions of  $Re_\lambda$ , as well as the resolution constraints at the small and large scales. The evolution of  $Re_\lambda$  is presented in Fig. 3(a), which shows a monotonic growth of the Reynolds number for all cases. The computational domain size constraint for the evolution of the large-scale structures, i.e., the unbounded growth of the integral length scale, is demonstrated in Fig. 3(b) by presenting the evolution of the integral length scale in the streamwise direction, defined as

$$\mathcal{L}(t) \equiv \frac{1}{u_1(\mathbf{x}, t)u_1(\mathbf{x}, t)} \int_0^\infty u_1(\mathbf{x}, t)u_1(\mathbf{x} + r\mathbf{e}_1, t) dr, \quad (15)$$

where  $\mathbf{e}_1$  is the unit vector in the  $x_1$  direction. This figure shows that for all cases, the integral length scale  $\mathcal{L}(t)$  grows monotonically [note that the integral length scale  $\mathcal{L}$  should not be confused with the linear operator symbol in Eq. (9)].

The resolution criterion for the small-scale structures is demonstrated in Fig. 3(c) by presenting  $\eta/\Delta x_2$ , where  $\eta \equiv (\nu^3/\epsilon)^{1/4}$  is the Kolmogorov microscale and  $\epsilon$  is the turbulent kinetic energy dissipation rate. It can be observed that although this quantity decreases monotonically, for all cases the criterion  $\eta/\Delta x_2 \geq 1.2$  is retained during the simulation time.

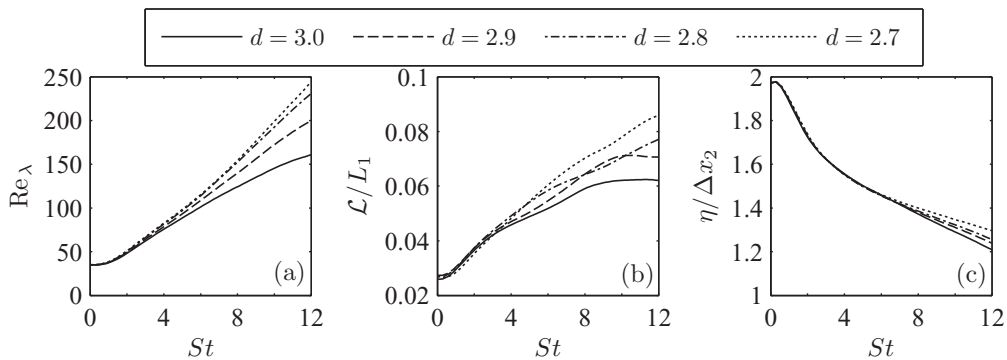


FIG. 3. Temporal evolution of (a) the Reynolds number based on the Taylor microscale  $Re_\lambda$ ; (b) the streamwise integral length scale  $\mathcal{L}$ , normalized by the computational domain size; (c) the Kolmogorov length scale  $\eta$  normalized by the grid spacing in the cross-stream direction  $\Delta x_2$ .

From these figures it can be observed that the fidelity of the simulations are maintained until  $St \leq 12$ . After this time, both resolution requirements, i.e.,  $\eta/\Delta x_2 \geq 1.2$  and  $d\mathcal{L}/dt \geq 0$ , will be violated simultaneously, which implies that within the considered resolution, the chosen simulation parameters yield maximum simulation window time. Interestingly, it can be observed that the window of time, over which the simulations retain resolution for large and small scales, increases by reduction of the Fourier dimension. This issue can be retrieved from Figs. 3(b) and 3(c), by comparing the evolutions of  $\mathcal{L}/L_1$  and  $\eta/\Delta x_2$  for the test case  $d = 2.7$  to those in the original problem  $d = 3$ .

#### IV. RESULTS

The DNS results are presented in the following: First, the impact of the variation of the Fourier dimension  $d$  on the overall HTSF evolution is discussed in Sec. IV A. Next, the sensitive dependence of the dynamics of the large and small scale structures on the variation of  $d$  is discussed in Secs. IV B and IV C, respectively. Finally, in Sec. IV D, the influence of  $d$  on the spectral energy transfer is investigated.

##### A. Overall flow field evolution

One of the most ubiquitous aspects of the HTSF evolution is the development of an enormous number of tangled, large- and small-scale streamwise vortical structures, which are generated through coupling between the turbulence and the mean shear flow. In Fig. 4, the impact of the variation of the Fourier dimension on this fundamental feature of the HTSF is visualized by comparing the proliferation of these large and small structures at different dimensions  $d$ .

Despite the lack of a clear definition for the small and large scales or eddies in physical space, the small scales are associated with the field of the velocity gradients while the large scales are characterized by the velocity field [1,30]. The velocity gradient includes both the symmetric part, i.e., the strain rate  $s_{ij} = (\partial u_i/\partial x_j + \partial u_j/\partial x_i)/2$ , and the asymmetric part, which is related to the vorticity  $\omega_i = \varepsilon_{ijk}\partial u_k/\partial x_j$  and  $\varepsilon_{ijk}$  denoting the alternating symbol. Since in a homogeneous field  $2s_{ij}s_{ij} = \overline{\omega_i\omega_i}$ , in this research the small-scale structures are probed based on the enstrophy field  $\omega^2$ .

Figures 4(a) and 4(b) demonstrate the impact of the dimensionality on the instantaneous state of the large-scale structures. In these figures, the snapshots of the turbulent kinetic energy isosurfaces  $q^2 \approx 1.7$  for the flow fields with  $d = 3.0$  and  $d = 2.7$ , at the well developed stage  $St = 10$ , are presented. In both dimensions large scale eddies appear as streaky structures, which are elongated in the streamwise direction [21,31]. A strong visual correlation between the instantaneous turbulent kinetic energy fields in  $d = 3.0$  and  $d = 2.7$  can be discerned, which implies that the dynamics of the large-scale structures are not significantly affected by the variation of the Fourier dimension.

Correspondingly, Figs. 4(c) and 4(d) demonstrate the impact of the dimensionality on the instantaneous state of the small-scale structures. In these figures, the snapshots of the enstrophy isosurfaces  $\omega^2 \approx 160$ , at the same circumstances of Figs. 4(a) and 4(b), are presented. Similar to the large-scale structures, it can be seen that as a result of the mean shear action, the initially incoherent vorticity blobs are stretched into the coherent, streamwise elongated vortex tubes. However, it can be observed that the reduction of the Fourier dimension substantially influences the small-scale structures.

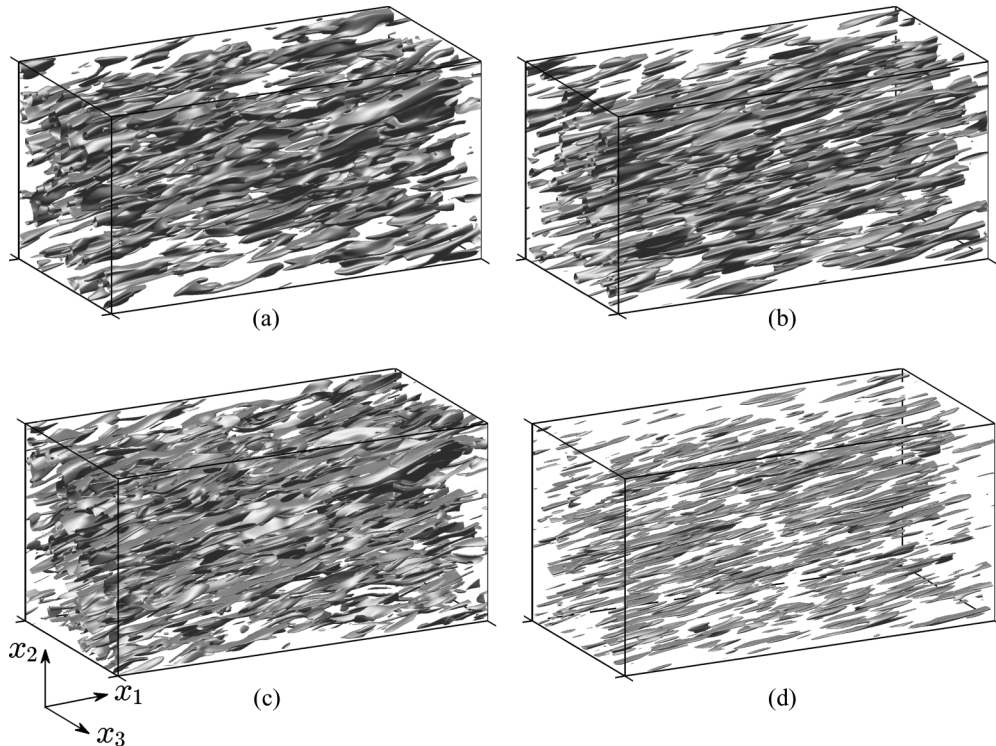


FIG. 4. The snapshots of the energy isosurfaces  $q^2 \approx 1.7$  of the flow fields for (a)  $d = 3.0$  and (b)  $d = 2.7$ . The snapshots of the enstrophy isosurfaces  $\omega^2 \approx 160$  of the flow fields for (c)  $d = 3.0$  and (d)  $d = 2.7$ . All flow fields at  $St = 10$ .

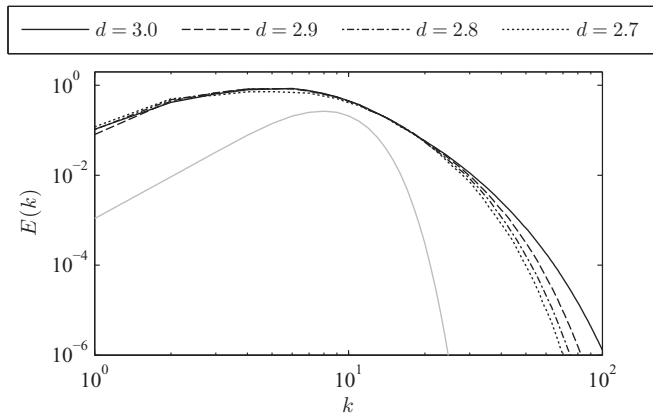


FIG. 5. The three-dimensional energy spectrum at  $St = 10$ , developed from a  $k^4$ -exponential initial energy spectrum, indicated by the grey curve.

The enstrophy field at  $d = 3.0$  shows highly convoluted and tangled vortical structures while in the flow field with  $d = 2.7$  the complexity of these structures is considerably reduced. The instantaneous state of the flow field structures with  $d = 2.9$  and  $2.8$  follow the observed trend (not shown).

The less granulated turbulent flow field structure at the lower Fourier dimension can be further investigated by considering the hampering effect of the dimension reduction on the level of the small-scale activity. This issue is examined in Fig. 5 based on the kinetic energy of the large and small scales. Since the flow field scales are intrinsically related to the Fourier space, the energy spectrum can provide an appropriate description for the kinetic energy of different scales. Figure 5 shows the three-dimensional energy spectrum of all cases at  $St = 10$ , developed from a  $k^4$ -exponential initial energy spectrum. Due to the modest range of the Reynolds number, neither of the spectra shows a discernible inertial subrange. This issue can be also clearly observed in Fig. 13, in which  $k$  independent spectral energy flux is not established.

Consistent with the visualization in Fig. 4, it can also be observed in Fig. 5 that for all cases, the infrared (low wave number) region of the spectra, which represents the kinetic energy of the large-scale structures, collapses fairly well. However, the ultraviolet (high wave number) region of the spectra shows steeper descent for the flow fields with lower dimensions. Therefore, although the kinetic energy of the large scales shows an almost insensitive dependence on the variation of the flow field dimension, the kinetic energy of the small scales declines as the Fourier dimension reduces.

Finally, the overall dynamics of the large and small scales are investigated in Fig. 6, by considering time evolutions of the turbulent kinetic energy  $q^{*2} \equiv q^2/q_0^2$  and the enstrophy  $\omega^{*2} \equiv \omega^2/\omega_0^2$ , normalized by their respective initial values. Figure 6(a) shows that the time evolution of the turbulent kinetic energy is slightly affected by the variation of the Fourier dimension. All test cases show an almost identical monotonically increasing turbulent kinetic energy evolution except for the test case with the lowest dimension  $d = 2.7$ , whose time evolution to some extent deviates from the other test cases after  $St \approx 6$ . The sensitive dependence of the turbulent kinetic energy evolution on the variation of the Fourier dimension can be further examined by considering its nondimensional growth rate, i.e.,  $\sigma_{eng} \equiv \dot{q}^2/(Sq^2)$ .

Approximately after  $St \approx 6$ , for all cases  $\sigma_{eng}$  evolves to an asymptotically constant value, which implies an approximately exponential growth for the turbulent kinetic energy, i.e.,  $q^{*2} \propto \exp(\sigma_{eng} St)$ . The dependency of the exponent growth rate on the dimension variation is plotted in the inset of Fig. 6(a). It can be observed that reduction of the Fourier dimension from  $d = 3.0$  to  $d = 2.7$  results in a 20% reduction of the turbulent kinetic energy growth rate.

Figure 6(b) shows the time evolution of the normalized enstrophy for all cases. Similar to the turbulent kinetic energy,  $\omega^{*2}$  also shows a monotonic increase during the flow field evolution. However, compared to  $q^{*2}$ , variation of the Fourier dimension shows a more pronounced influence on the time evolution of this quantity for  $St \gtrsim 6$ . This sensitive dependency

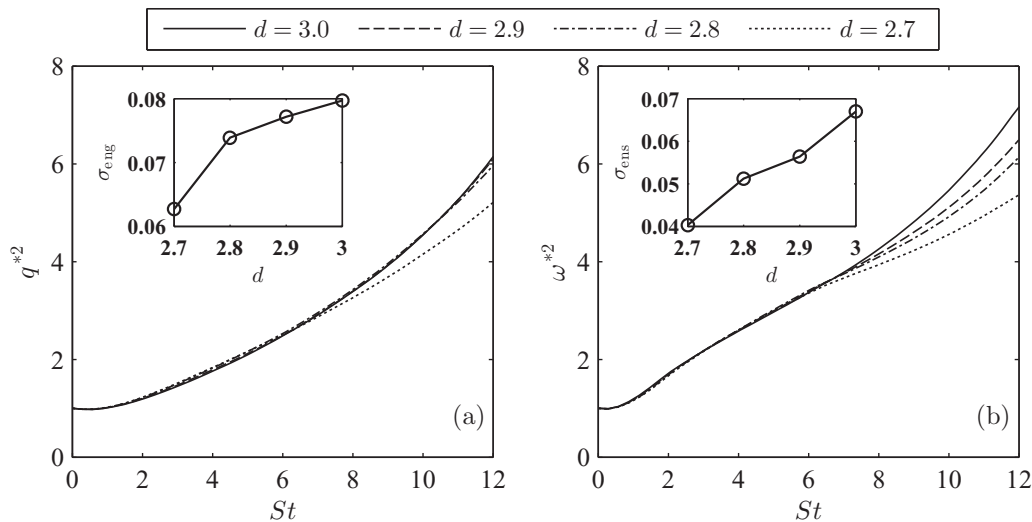


FIG. 6. Time evolutions of the normalized (a) turbulent kinetic energy  $q^{*2}$ , and (b) enstrophy  $\omega^{*2}$ . In the insets: the asymptotic values of the nondimensional growth rates of the (a) energy  $\sigma_{eng} \equiv \dot{q}^2/(Sq^2)$ , and (b) enstrophy  $\sigma_{ens} \equiv \dot{\omega}^2/(S\omega^2)$ .

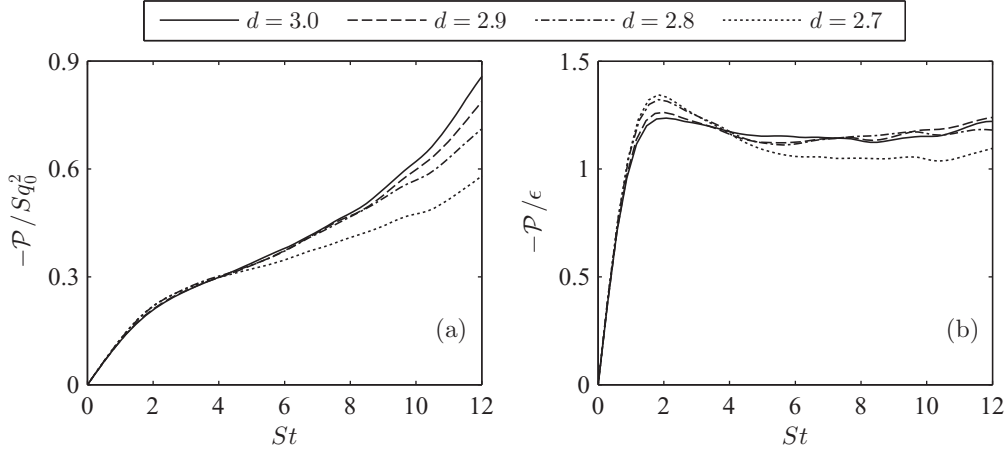


FIG. 7. Temporal evolution of (a) the normalized turbulent kinetic energy production  $-\mathcal{P}$  and (b) the ratio of the turbulent kinetic energy production to dissipation  $-\mathcal{P}/\epsilon$ .

is more investigated by considering the nondimensional growth rate of the enstrophy, i.e.,  $\sigma_{\text{ens}} \equiv \dot{\omega}^2 / (S\omega^2)$ .

Similar to the turbulent kinetic energy,  $\sigma_{\text{ens}}$  also develops to a constant evolution after  $St \approx 6$ , which implies an approximately exponential growth for the enstrophy. The asymptotic enstrophy growth rate exponent is presented in the inset of Fig. 6(b). Clearly, an approximately 40% reduction in the enstrophy growth rate can be observed, as the Fourier dimension reduces from  $d = 3.0$  to  $d = 2.7$ , i.e., almost two times the reduction of the turbulent kinetic energy growth rate.

### B. Turbulent kinetic energy

In this section, the dynamics of the large scales is further examined by considering the Reynolds stresses. The transport equation of the Reynolds stresses for the decimated field  $v_i(\mathbf{x}, t)$ , and  $p(\mathbf{x}, t)$  may be written as follows:

$$\frac{dR_{ij}}{dt} = \mathcal{P}_{ij} + \Pi_{ij} - \epsilon_{ij}, \quad (16)$$

where

$$R_{ij} \equiv \overline{P^D\{v_i v_j\}}, \quad \mathcal{P}_{ij} \equiv -R_{jk} \frac{\partial U_i}{\partial x_k} - R_{ik} \frac{\partial U_j}{\partial x_k},$$

$$\Pi_{ij} \equiv \overline{P^D\left\{p\left(\frac{\partial v_i}{\partial x_j} + \frac{\partial v_j}{\partial x_i}\right)\right\}}, \quad \epsilon_{ij} \equiv \overline{P^D\left\{2\nu \frac{\partial v_i}{\partial x_k} \frac{\partial v_j}{\partial x_k}\right\}}, \quad (17)$$

and  $P^D$  is the projection operator as indicated in Eq. (10). This equation implies that at each time iteration, the nonlinear terms are projected on the preselected set of the active Fourier modes. In Eqs. (16) and (17),  $\mathcal{P}_{ij}$  is the production term,  $\Pi_{ij}$  is the redistribution term, and  $\epsilon_{ij}$  denotes viscous dissipation. The governing equation for the turbulent kinetic energy is directly related to the trace of the Reynolds stress transport equation (16),

$$\frac{1}{2} \frac{dq^2}{dt} = \mathcal{P} - \epsilon, \quad (18)$$

where  $q^2 \equiv R_{ii}$  is the turbulent kinetic energy,  $\mathcal{P} \equiv \mathcal{P}_{ii}/2$  represents the turbulent kinetic energy production, and  $\epsilon \equiv \epsilon_{ii}/2$  is the turbulent kinetic energy dissipation.

Figure 7 presents time evolutions of the relevant terms in equation (18). In Fig. 7(a), a monotonically increasing evolution for  $\mathcal{P}$  can be observed, where the growth rate reduces as the flow field Fourier dimension decreases. Noting that in the homogeneous incompressible flow  $\epsilon = \nu\omega^2$ , the time evolution of the turbulent dissipation can also be retrieved from Fig. 6(b).

Figure 7(b) compares the time evolutions of the turbulent production and dissipation. It can be observed that for all cases, the ratio of these quantities approaches an asymptote  $\mathcal{P}/\epsilon \sim -1.2$ , which weakly depends on the Fourier dimension. This implies an almost similar sensitive dependence of the production and dissipation (enstrophy) on the variation of the Fourier dimension. As observed in Fig. 6, however, the variation of the Fourier dimension has a significantly smaller impact on the evolution of  $q^2$ , compared with  $\omega^2$ . This lower sensitivity could be explained based on the turbulent kinetic energy equation (18), in which the comparative variations of  $\epsilon$  and  $\mathcal{P}$ , as the Fourier dimensionality varies, tend to offset each other.

The evolution of the turbulent production can be further examined by noting that in the considered flow field configuration, this quantity may be written as  $\mathcal{P} = -S\rho_{12}\sqrt{R_{11}R_{22}}$ , where  $\rho_{12} = R_{12}/\sqrt{R_{11}R_{22}}$  is the only nonzero correlation coefficient. From the DNS results, it is found that after  $St \gtrsim 6$ , the correlation coefficient approaches an asymptotic value  $\rho_{12} = -0.581 \pm 0.003$ , independent from the Fourier dimension. This asymptotic value for the correlation coefficient is consistent with the previous results [32,33]. Therefore, the observed variability of the turbulent production evolution can be related to the sensitive dependence of the Reynolds stresses  $R_{11}$  and  $R_{22}$  on the Fourier dimension variation.

Considering an initially isotropic field, the evolution of the diagonal Reynolds stress components can be concisely written as

$$\frac{dR_{11}}{dt} = \Pi_{11} - \epsilon_{11} + \mathcal{P}_{11}, \quad \frac{dR_{22}}{dt} = \Pi_{22} - \epsilon_{22},$$

$$\frac{dR_{33}}{dt} = \Pi_{33} - \epsilon_{33}, \quad (19)$$

where different terms in the above equations are introduced in relations (17).

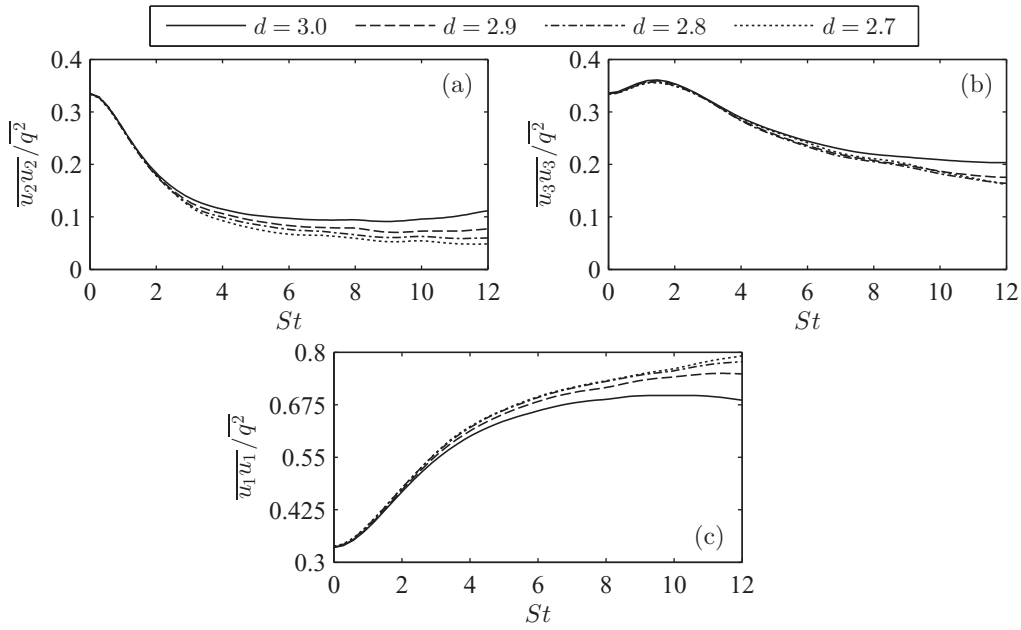


FIG. 8. Time evolution of three normalized diagonal components of the Reynolds stress tensor: (a) normal  $R_{22}/q^2$ , (b) spanwise  $R_{33}/q^2$ , and (c) streamwise component  $R_{11}/q^2$ .

Dynamics of Eqs. (19) may be briefly described as follows:  $R_{11}$  directly receives energy from the mean flow through the action of the mean shear on the turbulent field, represented by  $\mathcal{P}_{11}$ . Part of this energy is redistributed among different directions by diagonal terms of the pressure strain  $\Pi_{ij}$ , without affecting the overall turbulent kinetic energy. Finally, the distributed energy among different directions is dissipated by the corresponding diagonal components of  $\epsilon_{ij}$ , which appear as the energy sinks in the dynamical equations (19).

Figure 8 shows the time evolutions of the diagonal Reynolds stresses components, normalized by the turbulent kinetic energy. During long periods of time, it can be observed that these

quantities approach their approximately asymptotes. Figures 8(a) and 8(b), however, show that the asymptotic values for the normal  $R_{22}/q^2$  and spanwise  $R_{33}/q^2$  components decrease as the Fourier dimension decreases, while Fig. 8(c) shows an opposite trend for the streamwise component  $R_{11}/q^2$ . Since the reduction of the Fourier dimension has a hampering effect on the viscous dissipation, including  $\epsilon_{22}$  and  $\epsilon_{33}$ , the lower asymptotic values of  $R_{22}/q^2$  and  $R_{33}/q^2$  could be related to the behavior of their source terms, i.e.,  $\Pi_{22}$  and  $\Pi_{33}$ .

Figure 9 demonstrates the impact of the variation of the Fourier dimension on the diagonal components of the pressure strain. This figure signifies the central role of the

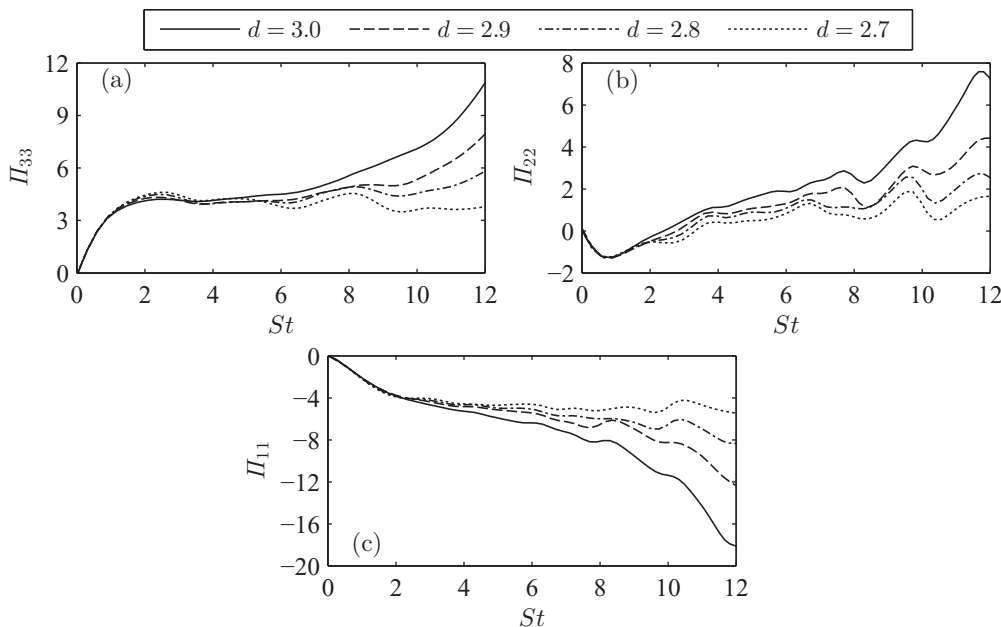


FIG. 9. Time evolutions of the pressure-strain diagonal components (a)  $\Pi_{33}$ , (b)  $\Pi_{22}$ , and (c)  $\Pi_{11}$ .

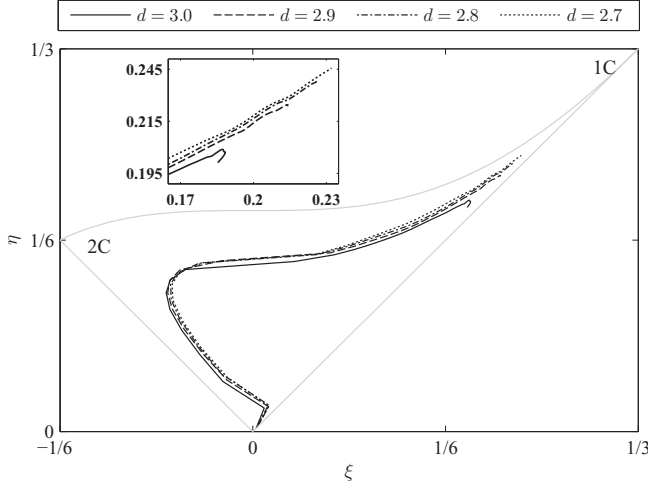


FIG. 10. Plot of the Lumley triangle in the plane of invariants ( $\eta$ ,  $\xi$ ) of the Reynolds stress anisotropy tensor. The vertices correspond to two-component (2C) and one-component (1C) turbulence, as indicated. The inset in the upper side presents the final stage of the anisotropy levels for all cases.

pressure strain in energy redistribution. Both  $\Pi_{22}$  and  $\Pi_{33}$  are dominantly positive while  $\Pi_{11}$  is entirely negative throughout the flow field evolution. Therefore,  $\Pi_{11}$  extracts energy from the streamwise component  $R_{11}$  and redistributes it between the cross stream  $R_{22}$  and the spanwise  $R_{33}$  components, via  $\Pi_{22}$  and  $\Pi_{33}$ . From this figure, the suppressing effect of the lower Fourier dimension on the energy redistribution process can be observed.

Figures 9(a)–9(c) clearly show that the magnitudes of all  $\Pi_{11}$ ,  $\Pi_{22}$ , and  $\Pi_{33}$  reduce as the Fourier dimension reduces. As it can be observed from Eq. (19), reductions of the source terms  $\Pi_{22}$  and  $\Pi_{33}$  impede the growth of  $R_{22}$  and  $R_{33}$  while reduction of the sink term  $\Pi_{11}$  intensifies the growth of  $R_{11}$ . Nevertheless, the net effect of the countervariations of  $R_{22}$  and  $R_{11}$  is the reduction of the turbulent production term  $\mathcal{P} = -S\rho_{12}\sqrt{R_{11}R_{22}}$ , as observed in Fig. 7(a).

Moreover, the main contribution to the turbulence isotropization process comes from the dynamics of the pressure-strain term. Therefore, one might expect the level of the large-scale anisotropy to be also influenced by the variation of the Fourier dimension. The large-scale anisotropy can be quantified based on the invariants of the anisotropy tensor, i.e.,  $II = b_{ij}b_{ji}/2$  and  $III = b_{ij}b_{jk}b_{ki}/3$ , where  $b_{ij} = R_{ij}/q^2 - \delta_{ij}/3$ .

Figure 10 shows the flow field evolution in a plane spanned by  $3\eta^2 = II$  and  $2\xi^3 = III$ . It can be seen that all trajectories start from the initial isotropic state and finally move towards the one-component corner. During this final approach, all trajectories are equidistantly located between the upper and lower boundaries, which respectively represent the rodlike and the two-component disklike turbulence structures. This indicates that the kinematics of the longitudinal vortex is simultaneously compressed in the cross-stream direction and stretched in both the streamwise and spanwise directions [22].

The upper inset in Fig. 10 shows the final stage of the anisotropy levels for all cases. It can be observed that

by lowering the Fourier dimension, the final stage of the anisotropy is more stretched towards the one-component corner, i.e., 1C point. Indeed, less effective energy distribution in flow fields with lower dimensions prevents developments of  $R_{22}$  and  $R_{33}$ , resulting in a more rodlike structure of the Reynolds stress tensor.

### C. Vorticity dynamics

In this section, the dynamics of the small scales is examined by considering the fluctuating enstrophy. Denoting the fluctuating vorticity of the decimated field by  $\omega_i \equiv P^D\{\epsilon_{ijk}\partial u_j/\partial x_k\}$  the transport equation of the decimated fluctuating enstrophy  $\omega^2 \equiv P^D\{\omega_i\omega_i\}$  for HTSF may be written as follows:

$$\frac{d}{dt}\left(\frac{\omega^2}{2}\right) = \underbrace{P^D\{\omega_i\omega_j S_{ij}\}}_{VS_{\text{Turb}}} + \underbrace{P^D\{\omega_i\omega_j\}S_{ij}}_{VS_{\text{Mean}}} - \underbrace{P^D\left\{v\frac{\partial\omega_i}{\partial x_j}\frac{\partial\omega_i}{\partial x_j}\right\}}_{\epsilon_{\text{ens}}}. \quad (20)$$

Figure 11 presents time evolutions of the different terms of Eq. (20). In Fig. 11(a), it can be observed that for all cases,  $VS_{\text{Turb}}$  undergoes a monotonic growth, however, its growth rate significantly decreases as the Fourier dimension reduces. This sensitive dependence originates from the dominant contribution of the small-scale dynamics to this vortex stretching mechanism.

In contrast to  $VS_{\text{Turb}}$ , Fig. 11(b) shows that after an initial rise during the transitional period,  $VS_{\text{Mean}}$  develops into a stationary evolution, independent of the Fourier dimension. This trend is expected because this vortex stretching mechanism is governed by the dynamics of the large-scale structures, which are relatively insensitive to the variations of the Fourier dimension.

Figure 11(c) shows the time evolution of the enstrophy dissipation. For all cases, a close similarity between time evolutions of  $\epsilon_{\text{ens}}$  and  $VS_{\text{Turb}}$  in Fig. 11(a) can be discerned. This observed correlative behavior of  $VS_{\text{Turb}}$  and  $\epsilon_{\text{ens}}$  in Figs. 11(a) and 11(c) implies that the dissipation adjusts itself to the vortex stretching process  $VS_{\text{Turb}}$ , which is closely related to the concept of the energy cascade in the physical space. This issue might be further quantified by considering the skewness of the velocity derivative, which is related to the energy transfer based on the Kolmogorov's four-fifths law [34]. Moreover, Gaussian departure of the small-scale statistics and their intermittency can also be measured by this quantity.

For the HSTF configuration, a generalization of the velocity-derivative skewness is defined as [35]

$$S_{u_x} = \frac{\frac{1}{3}\overline{(\partial u_i/\partial x_i)^3}}{\left[\frac{1}{3}\overline{(\partial u_j/\partial x_j)^2}\right]^{3/2}}, \quad (21)$$

where the summation convention has been adopted. The time evolution of this quantity is demonstrated in Fig. 12. The sensitive dependence of the  $S_{u_x}$  on the variation of the Fourier dimension can be clearly retrieved from this figure. It can be observed that for long periods of time, this quantity tends to develop into a constant level evolution.

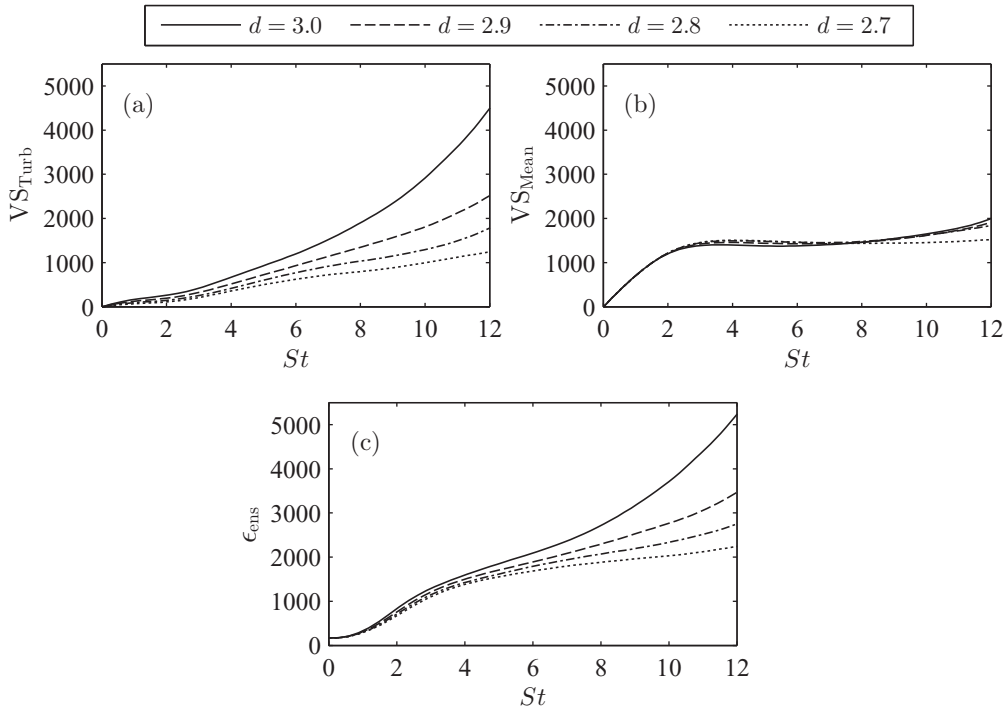


FIG. 11. Time development of different enstrophy dynamic terms. The time evolutions of (a) the vortex stretching  $VS_{Turb}$ , (b) the vortex stretching  $VS_{Mean}$ , and (c) the enstrophy dissipation  $\epsilon_{ens}$ .

However, the magnitude of this asymptotic state decreases as the Fourier dimension reduces. Therefore, the reduction of the Fourier dimension results in the reduction of the energy transfer, as well as the small-scale intermittency and departure from the Gaussian statistics. This trend is in agreement with substantial different small-scale statistical characteristics in two- and three-dimensional turbulences, where the latter is characterized by the small-scale intermittency whereas the former shows some indications of the small-scale Gaussianity.

#### D. Spectral energy transfer

Since the vortex stretching is equivalent to the intensification of the velocity derivatives, this process can be considered as the manifestation of the spectral energy transfer in physical space. In Sec. IV C, it was observed that the main vortex stretching mechanism significantly decreases as the Fourier dimension reduces, which leads to the demotion of the small-scale activities. In this section, this reduction of the downward energy transfer is investigated.

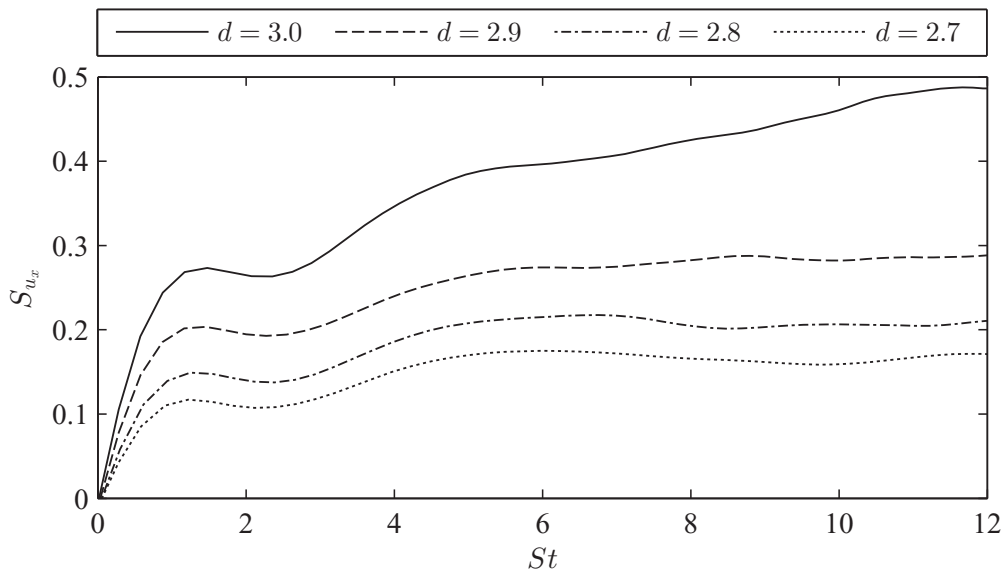


FIG. 12. Time development of the velocity derivative skewness  $S_{u_x}$ .

The concept of the energy transfer mechanism is intrinsically relevant in Fourier space, where the ‘‘scale’’ can be rigorously defined. Two quantities of primary importance for describing the energy transfer mechanism are the spectral energy transfer  $T(k)$  and the spectral energy flux  $\Pi(k)$ .

The spectral energy transfer  $T(k)$  represents the contribution of the nonlinear term of the Navier-Stokes equation to the time evolution of the energy spectrum  $E(k)$ . It quantifies the energy transfer rate from all wave numbers to a specific wave number  $k$ . This term is related to the Fourier transformation of the nonlinear term of the Navier-Stokes equation as follows:

$$T(k) = \int_{|\mathbf{k}'|=k} \int_{\mathbf{p}} \int_{\mathbf{q}} S(\mathbf{k}'|\mathbf{p}, \mathbf{q}) \delta(\mathbf{k}' - \mathbf{p} - \mathbf{q}) d\mathbf{p} d\mathbf{q} d\mathbf{k}'. \quad (22)$$

Here,  $\delta(\mathbf{k})$  is the vector Dirac  $\delta$  function, and  $S(\mathbf{k}'|\mathbf{p}, \mathbf{q})$  is the triad transfer function. For the decimated flow, this function, which presents a mode-to-mode energy transfer rate, may be expressed as

$$S(\mathbf{k}'|\mathbf{p}, \mathbf{q}) = -\text{Im}\{[\mathbf{k}' \cdot \hat{\mathbf{u}}^D(\mathbf{q})][\hat{\mathbf{u}}^D(\mathbf{p}) \cdot \hat{\mathbf{u}}^D(\mathbf{k}')] \} \\ - \text{Im}\{[\mathbf{k}' \cdot \hat{\mathbf{u}}^D(\mathbf{p})][\hat{\mathbf{u}}^D(\mathbf{q}) \cdot \hat{\mathbf{u}}^D(\mathbf{k}')] \}, \quad (23)$$

where  $\text{Im}$  denotes the imaginary part. The decimated Fourier coefficients are defined as  $\hat{\mathbf{u}}^D(\mathbf{k}) \equiv \alpha(\mathbf{k})\hat{\mathbf{u}}(\mathbf{k})$ , in which  $\alpha(\mathbf{k})$  are independent, prespecified, time-frozen random coefficients (11) (note that  $\mathbf{k}'$  should not be confused with the wave vector in the laboratory reference). The first (second) term in Eq. (23) represents energy transfer from mode  $\mathbf{p}$  (or  $\mathbf{q}$ ) to mode  $\mathbf{k}'$  with mode  $\mathbf{q}$  (or  $\mathbf{p}$ ) acting as the mediator. Similarly, the spectral energy flux, defined as

$$\Pi(k) = - \int_0^k T(k') dk' \\ = - \int_{|\mathbf{k}'| \leq k} \int_{\mathbf{p}} \int_{\mathbf{q}} S(\mathbf{k}'|\mathbf{p}, \mathbf{q}) \delta(\mathbf{k}' - \mathbf{p} - \mathbf{q}) d\mathbf{p} d\mathbf{q} d\mathbf{k}', \quad (24)$$

provides the energy transfer rate from all scales below  $k$  to those above  $k$ .

Figure 13(a) shows the spectral energy transfer function and flux for all cases at  $St = 10$ . It can be observed that  $T(k)$  is negative (positive) in the low (high) wave number region, which indicates the prevalence of the forward energy cascade for all cases. However, both negative and positive peaks of the energy transfer reduce as the Fourier dimension reduces.

Corresponding energy flux  $\Pi(k)$  is presented in Fig. 13(b). Due to the moderate Reynolds number during the flow field evolution, neither of the test cases shows the constant level energy flux. The forward direction of the spectral energy transfer can also be retrieved from the dominantly positive  $\Pi(k)$  throughout the whole range of the spectrum. However, consistent with the behavior of  $T(k)$ , reduction of the Fourier dimension leads to the reduction of the peak of the energy flux, which for all cases occurs at  $k \approx 13$ . This issue is better visualized in the inset of Fig. 13(b), which shows that reduction of the Fourier dimension from  $d = 3.0$  to  $d = 2.7$  results in an almost 50% reduction in the maximum spectral energy flux. Therefore, the spectral energy transfer is significantly impeded as the Fourier dimension reduces. As a result of this blockage of the forward energy transfer, the small-scale activities are

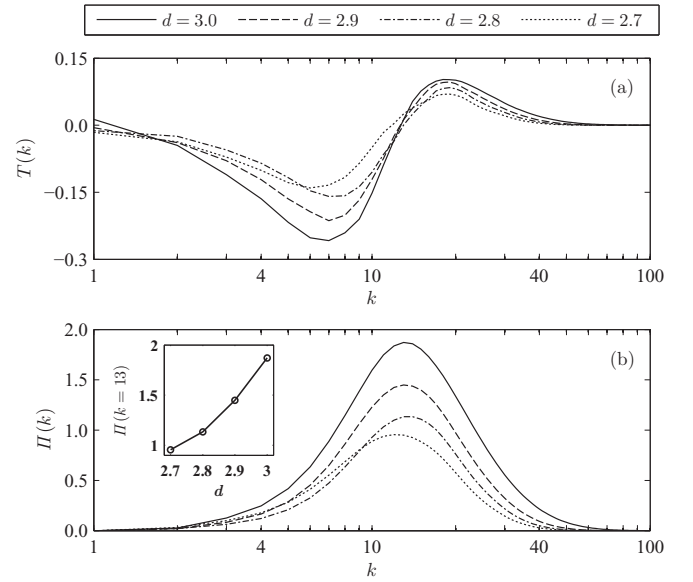


FIG. 13. (a) The spectral energy transfer  $T(k)$ , and (b) the spectral energy flux  $\Pi(k)$  for all test cases at  $St = 10$ . The inset of (b) presents the maximum of the energy flux  $\Pi(k)$  vs the flow field dimension  $d$ .

strongly hampered, which in turn leads to a faster decay of the ultraviolet part of the energy spectrum in Fig. 5.

The sensitive dependence of  $\Pi(k)$  on the variation of the flow field dimension can be further inspected by considering the following flux splitting:

$$\Pi(k) = \Pi^+(k) - \Pi^-(k), \\ \Pi^+(k) = \frac{1}{2} \int_{|\mathbf{k}'|=k} d\mathbf{k}' \int_0^{|\mathbf{q}|=k} \int_0^{|\mathbf{p}|=k} S(\mathbf{k}'|\mathbf{p}, \mathbf{q}) d\mathbf{p} d\mathbf{q}, \\ \Pi^-(k) = \frac{1}{2} \int_0^{|\mathbf{k}'|=k} d\mathbf{k}' \int_{|\mathbf{q}|=k} \int_{|\mathbf{p}|=k} S(\mathbf{k}'|\mathbf{p}, \mathbf{q}) d\mathbf{p} d\mathbf{q}, \quad (25)$$

where the wave vectors  $\mathbf{p}$ ,  $\mathbf{q}$ , and  $\mathbf{k}'$  are subjected to the triangle constraint.  $\Pi^+(k)$  presents the total rate of energy gain in the range  $k' > k$  due to the triad interactions with  $p, q < k$ , while  $\Pi^-(k)$  denotes the total rate of the energy loss in the range  $k' < k$  due to the triads with  $p, q > k$  [6]. In this research, these quantities are evaluated based on the coarse-grained shell-to-shell energy transfer function, which will be shortly introduced.

Figure 14 depicts  $\Pi^\pm(k)$  for all cases at  $St = 10$ . It can be clearly observed that the magnitudes of both  $\Pi^+(k)$  and  $\Pi^-(k)$  reduce as the Fourier dimension reduces. However, the variation of the Fourier dimension has a considerably higher impact on the  $\Pi^+(k)$ , as compared to the  $\Pi^-(k)$ . Therefore, the observed reduction of the total energy flux  $\Pi(k)$  in Fig. 13(b) mainly originates from the reduction of  $\Pi^+(k)$ , as the active Fourier set is reduced.

The observed dependency of the energy transfer mechanisms  $T(k)$  and  $\Pi(k)$  on the Fourier dimension can be further investigated by analyzing their Eqs. (22) and (24). Considering the spectral energy transfer  $T(k)$  for instance, its Eq. (22) may be written as the Riemann summation  $T(k) = (\delta k)^3 \sum_{|\mathbf{k}'|=|\mathbf{p}+\mathbf{q}|} S(\mathbf{k}'|\mathbf{p}, \mathbf{q})$ , where, as already introduced,  $(\delta k)^3$  represents the volume of the differential spectral element.

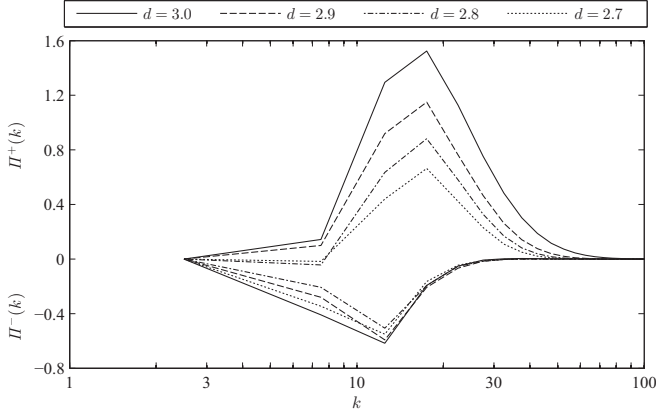


FIG. 14. Splitting energy flux  $\Pi(k)$  into two components  $\Pi^+(k)$  and  $\Pi^-(k)$  for all test cases at  $St = 10$ .  $\Pi^+(k)$  appears with positive values while  $\Pi^-(k)$  takes negative value, both contributing to the forward energy flux.

Here, summation takes place over all triads which can be formed among the set of active Fourier modes. This representation clearly shows that the variation of  $T(k)$  can originate from variations of (a) the number of the active triads, and (b) the magnitude of the triad transfer function  $S(\mathbf{k}|\mathbf{p},\mathbf{q})$ , as the Fourier dimension varies.

With respect to the first issue, the number of the active Fourier modes is proportional to the volume of the  $d$ -dimensional sphere,  $K^d$ , where  $K$  is the relevant spectral radius, i.e., the grid resolution. The number of the corresponding triads, which is proportional to the three-combination subset of these active modes, is approximately  $K^{3d}$ . Therefore, as the Fourier dimension decreases, the number of the active triads which contribute to the energy transfer process, and consequently  $T(k)$ , decreases.

This reduction of the energy transfer results in the energy deprivation of the downstream Fourier modes, which in turn influences the magnitude of the triad transfer function  $S(\mathbf{k}|\mathbf{p},\mathbf{q})$ . This interplay, which is related to the second issue, can be investigated by considering the impact of the variation

of the Fourier dimension on the course-grained triad transfer function  $\widehat{S}(l|n,m)$ .

Similar to  $S(\mathbf{k}|\mathbf{p},\mathbf{q})$ , the course-grained triad transfer function  $\widehat{S}(l|n,m)$  represents the energy transfer into shell  $l$  due to all interactions between the Fourier modes in shells  $n$  and  $m$ , subjected to the triangle constraint. Although, as a result of this coarse graining procedure, some of the detailed information is lost,  $\widehat{S}(l|n,m)$  still preserves the physical relevance of the original triad transfer function [36].

To evaluate  $\widehat{S}(l|n,m)$ , the wave-number space is divided into concentric spherical shells, here with shell thickness  $\Delta k = 3$ . Using band-filtered velocity field, the coarse-grained triad transfer function is defined as

$$\widehat{S}(l|n,m) = \sum_{\substack{k_l \leq |\mathbf{k}| < k_{l+1} \\ p_n \leq |\mathbf{p}| < p_{n+1} \\ q_m \leq |\mathbf{q}| < q_{m+1}}} S(\mathbf{k}|\mathbf{p},\mathbf{q}). \quad (26)$$

Due to the considerable variations in magnitude of  $\widehat{S}(l|n,m)$  over different shells, a more appropriate description can be obtained by the following normalization [37]:

$$\bar{S}(l|n,m) = \frac{\widehat{S}^-(l|n,m)}{S_{\min}} + \frac{\widehat{S}^+(l|n,m)}{S_{\max}}, \quad (27)$$

where  $S_{\min}$  and  $S_{\max}$  represent the minimum and maximum of  $\widehat{S}(l|n,m)$ , respectively. The positive and negative parts of the energy transfer function in the above normalization are defined as

$$\widehat{S}^+(l|n,m) = \begin{cases} \widehat{S}(l|n,m) & \text{if } \widehat{S}(l|n,m) \geq 0, \\ 0 & \text{otherwise,} \end{cases} \quad (28)$$

and similarly

$$\widehat{S}^-(l|n,m) = \begin{cases} \widehat{S}(l|n,m) & \text{if } \widehat{S}(l|n,m) \leq 0, \\ 0 & \text{otherwise.} \end{cases} \quad (29)$$

Figures 15(a) and 15(b) show the normalized course-grained triad transfer function,  $\bar{S}(l|n,m)$ , for two cases  $d = 2.7$  and  $d = 3.0$ , at the wave number  $k = 50$ , at  $St = 10$ . Comparing these figures, qualitatively similar regions in  $(k_p, k_q)$  planes can be discerned, which may be concisely

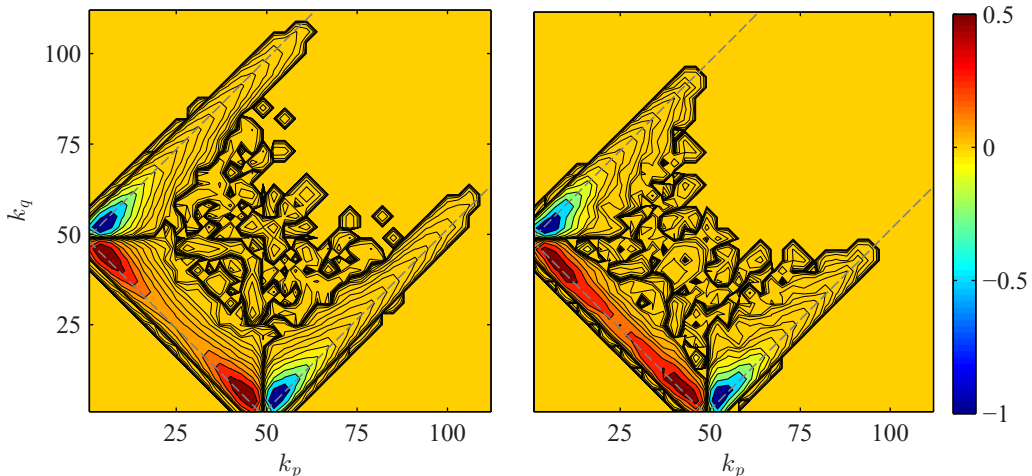


FIG. 15. The normalized triad energy transfer function  $\bar{S}(l|n,m)$  for  $k = 50$ . (a)  $d = 2.7$ , and (b)  $d = 3.0$ , at  $St = 10$ . The contour levels are  $\pm 1/2^m$ ,  $m = 0, \dots, 20$  that are the same for all pictures.

describes as follows (a more complete description can be found in Refs. [36–39]): first, high intensity regions, in which the contours appear as a dipole and are localized at the corners of the rectangular area; second, mainly negative low intensity regions, which are extended along  $|k_p - k_q| = k$  boundaries of the rectangular area; finally, low intensity negative and positive islands, which are irregularly scattered throughout the central part of the rectangular area.

Low intensity regions along  $|k_p - k_q| = k$  boundaries mainly represent weak forward nonlocal energy exchange while those in the central part of the rectangular area contribute to both weak forward and backward energy exchange.

However, the main contribution to the energy exchange comes from the high intensity regions, located at the corners of the rectangular area. These dominant energy exchanges take place between two wave numbers of similar size, i.e.,  $k_p \approx k$  ( $k_q \approx k$ ), and a considerably smaller wave number as the mediator, i.e.,  $k_q \approx 0$  ( $k_p \approx 0$ ). This combination indicates a local energy exchange through a nonlocal, elongated triad (this issue will be further investigated using locality function). Moreover, it can be observed that in these regions, the coarse-grained triad transfer function is strictly positive [ $\widehat{S}(l|n, m) \approx S_{\max}$ ] below the wave number  $k$ , and strictly negative, [ $\widehat{S}(l|n, m) \approx S_{\min}$ ] above the wave number  $k$ . Therefore, high intensity regions contribute to the forward energy exchange between adjacent wave numbers.

Despite above-mentioned similarities in Figs. 15(a) and 15(b), a variation of the Fourier dimension, qualitatively and quantitatively, influences  $\widehat{S}(l|n, m)$ , specifically in the high intensity regions. Quantitatively, it is found that the extrema of the triad transfer function, i.e.,  $S_{\min}$  and  $S_{\max}$ , show one order of magnitude reduction,  $\mathcal{O}(10)$ , as the Fourier dimension reduces from  $d = 3.0$  to  $d = 2.7$ . With respect to the energy transfer function  $T(k)$ , this observation signifies that besides reduction of the number of the active triads, the magnitude of  $S(\mathbf{k}|\mathbf{p}, \mathbf{q})$ , measured by  $S_{\min}$  and  $S_{\max}$ , is also tremendously decreased.

This reduction of the magnitude of the triad transfer function is consistent with the observed behavior of the fractally decimated Burgers equation. Similar to the Navier-Stokes equation, in the one-dimensional Burgers equation mode-to-mode energy transfer appears in triads. It has been observed that reduction of the Fourier dimension of the one-dimensional Burgers equation results in the significant loss of the phase coherency amongst triad phases and consequently depletion of the energy transfer [40].

By comparing Figs. 15(a) and 15(b), qualitative differences between their respective high intensity regions can also be discerned. It can be observed that in contrast to the flow field with  $d = 3.0$ , in which the dominant energy exchange is acutely localized in the corners of the rectangular area, the flow field with lower dimension  $d = 2.7$  shows a quite extended interaction region along the rectangular boundary  $|k_p + k_q| = k$ . Geometrically speaking, the dominant energy exchange in the former case takes place between  $k_p \approx k$  with mediator wave number  $k_q \approx 0$ , i.e., the local energy transfer through the nonlocal triads, while in the latter case between  $k_p \approx k$  through mediator wave number  $k_q \approx 0$ , i.e., energy transfer through less nonlocal triads.

This elongation of the interaction region along the rectangular boundary  $|k_p + k_q| = k$  can be further explained as follows.

The energy transfer into an eddy corresponding to the wave number  $k$  is proportional to the imposed strain fields on it, from all other eddies, which may be presented by  $[\int \kappa^2 E(\kappa) d\kappa]^{1/2}$  [25]. If one assumes a power law spectrum  $E(\kappa) \propto \kappa^{-m}$  for eddies in the positive region along the rectangular boundary  $|k_p + k_q| = k$  with  $1 < m \leq 3$  [13], the energy transfer into the wave number  $k$  can be approximated as  $[\int_0^k \kappa^{2-m} d\kappa]^{1/2}$ .

The integrand represents the contribution of different modes  $0 < \kappa < k$  along the  $|k_p + k_q| = k$  to energy transfer into mode  $k$ . It can be observed that as the exponent  $m$  increases (decreases), the contributions of the distant modes  $\kappa \ll k$  from this region to the total energy exchange become more (less) pronounced, which can be interpreted as the energy transfer through local (nonlocal) triads.

Therefore, the sequence of events might be considered as follows. As the Fourier dimension decreases, the efficiency of the spectral energy transfer reduces, which leads to the deprivation of the small-scale kinetic energy. This hampering effect results in a faster decline of the corresponding energy spectrum, i.e., increase of  $m$  in view of the model energy spectrum.

Besides the above-mentioned qualitative discussion, the impact of the Fourier dimension variation on the locality of the energy transfer triads can also be quantitatively investigated, using the energy transfer locality function. This quantity provides a measure for the disparity of the interacting scales [6]. In order to separate the local and nonlocal interactions, different triads are parametrized based on the ratio of the smallest to the middle wave number, here denoted by  $v$ . The energy transfer locality function represents the fraction of the total nonlinear energy transfer that is due to all triad interactions in which the ratio of the smallest to the middle wave number is greater than  $v$ , and computed as follows [38]:

$$W(v) = \frac{\sum_{k' \geq k} \sum_{v \geq r} T(k'|p, q)}{\sum_{k' \geq k} \sum_{p, q} T(k'|p, q)}, \quad v = \frac{\min(k', p, q)}{\text{mid}(k', p, q)}. \tag{30}$$

In Fig. 16, the locality function is plotted for all cases at  $St = 10$  and  $k = 50$ , using the coarse-grained transfer

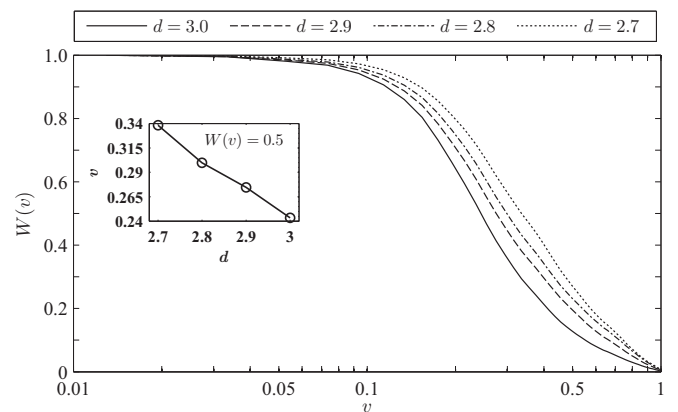


FIG. 16. The energy transfer locality function for all test cases at  $St = 10$  and  $k = 50$ . The inset presents the variation of the locality of triads involved in 50% energy transfer.

function. Overall, it can be observed that the contribution of the nonlocal triads to the turbulent kinetic energy exchange becomes more pronounced as the Fourier dimension increases. More precisely, it can be observed in the inset that half of the total energy transfer is accomplished by the triad interactions in which the ratio of the smallest wave number to the middle one is less than 0.34, 0.30, 0.27, and 0.24 at  $d = 2.7, 2.8, 2.9,$  and  $3,$  respectively. This indicates that the involved triads become more and more elongated as the Fourier dimension increases. As already discussed, this reduction of the triadic locality by increasing the Fourier dimension is also visualized in the corners of the rectangles in Figs. 15(a) and 15(b).

It should be noted that although mode-to-mode energy exchanges through nonlocal triads are extremely larger than those for local triads, the dominant contribution to the spectral energy flux comes from local triadic interactions [41]. Indeed, through the integration (24) or (22), larger cancellations occur among contributions from nonlocal triads, compared to those from local triads [42,43]. The higher scale locality of the energy transfer at a lower Fourier dimension in Fig. 16 implies that the fractal decimation results in a further cancellation of nonlocal contributions.

Moreover, as can be retrieved from Fig. 15, the nonlocal triads occupy a small fraction of the Fourier space volume compared to the local triads [44]. Therefore, the cumulative effects of the extremely larger number of the local triads overwhelm the contribution of the nonlocal triads in the above-mentioned integrations. However, to correctly capture this dominant effect of the local triads from a band-filtered velocity field with constant bandwidth on the linear scale, it is required to use band-pass filters with very broad spectral support [45,46]. From Fig. 16, one might interpret the fractal Fourier decimation as a filtering with a nonlocal kernel, whose spectral support is related to the fractal dimension  $d$ .

Fourier decimation can also influence the action of the mean shear on the turbulence. In the homogeneous shear flow, there is a contentious energy supply into the turbulent field, through the interaction of the mean shear with the turbulent flow. It is found that for all cases, the production term  $\mathcal{P}_{11}$  injects energy into the low wave number modes, dominantly within  $0 < k \lesssim 10$ . As a result of this direct energy injection, all the local and nonlocal triads with at least one mode in this region become more energetic than the other triads. Since this energy is directly received by the streamwise component of the fluctuations [see Eq. (19)], mean shear also induces anisotropy on the large-scale structures. This large-scale anisotropy can be directly transferred to the small-scale dynamics through the energized nonlocal triads. Due to this distant coupling, the dissipative scale of the HTSF can also show a significant level of the anisotropy.

However, this process can be significantly influenced by the Fourier decimation. As observed in Fig. 16, the energy transfer nonlocality reduces as the Fourier dimension reduces, which can hamper the direct induction of the anisotropy on the small-scale structures. Therefore, in contrast to the large-scale anisotropy, the small-scale anisotropy reduces as the Fourier dimension reduces. This issue can also be observed in Fig. 12, which shows the lower level of the velocity derivative skewness for the flow field with lower Fourier dimension.

## V. CONCLUSIONS

The impact of the variation of the flow field dimensionality on the temporal evolution of an incompressible homogeneous turbulent shear flow is investigated by conducting different direct numerical simulations (DNSs). The Fourier dimension is varied within  $2.7 \leq d \leq 3.0$ , by systematically reducing the degrees of freedom of the Navier-Stokes equation based on the fractal Fourier decimation method. Consistent with the previous studies, it is found that reduction of the Fourier dimension has a suppressive effect on the dynamics of both large and small-scale structures. However, evolution of the small-scale structures shows higher sensitivity to the variation of the Fourier dimension, compared to that of the large-scale structures.

Dynamics of the large-scale structures is investigated based on the time evolution of the turbulent kinetic energy. Developments of both kinetic energy production and dissipation, which are turbulent central mechanisms, are significantly hampered as the Fourier dimension reduces. Nevertheless, the time evolution of their ratio approaches an asymptote  $\mathcal{P}/\epsilon \sim -1.2$ , which weakly depends on the Fourier dimension. Therefore, the energy balance between large and small scales is not significantly affected by the modifications of the triad-to-triad energy transfer mechanism. The energy distribution among different diagonal components of the Reynolds stress is also hindered by the reduction of the Fourier dimension, which in turn increases the level of the large-scale flow field anisotropy.

Dynamics of the small-scale structures is investigated based on the vorticity dynamics. In all dimensions, the vorticity dynamics is dominantly governed by the interplay between the fluctuating vortex stretching mechanism and the enstrophy dissipation. The monotonical growth of both quantities, however, is significantly suppressed as the Fourier dimension reduces. The reduction of the vortex stretching process results in a lower level of small-scale intermittency as well as the lesser a departure from the Gaussian statistics. Within the considered range of dimensions, the energy transfer mechanism indicates strictly forward energy cascade process. However, similar to the vortex stretching process, this forward spectral energy transfer is significantly impeded by the reduction of the Fourier dimension. As a result of this energy blockage, the activities of the small-scale structures are suppressed, which affects the high wave number part of the energy spectrum: the lower the Fourier dimension, the steeper the decay of the ultraviolet region of the energy spectrum.

By splitting the spectral energy flux into  $\Pi^-(k)$  and  $\Pi^+(k)$ , it is found that the magnitude of both components decreases as the Fourier dimension reduces. However,  $\Pi^+(k)$  shows considerably higher decline compared to  $\Pi^-(k)$  as the Fourier dimension reduces.

By reconstructing the course-grained triad transfer function, modifications in the triad-to-triad nonlinear energy transfer mechanism is also investigated. It is found that for all cases the energy exchange dominantly takes place between two wave numbers of similar size and one considerably smaller wave number as the mediator. However, the reduction of the Fourier dimension quantitatively and qualitatively influences this dominant energy exchange mechanism. First, the intensity

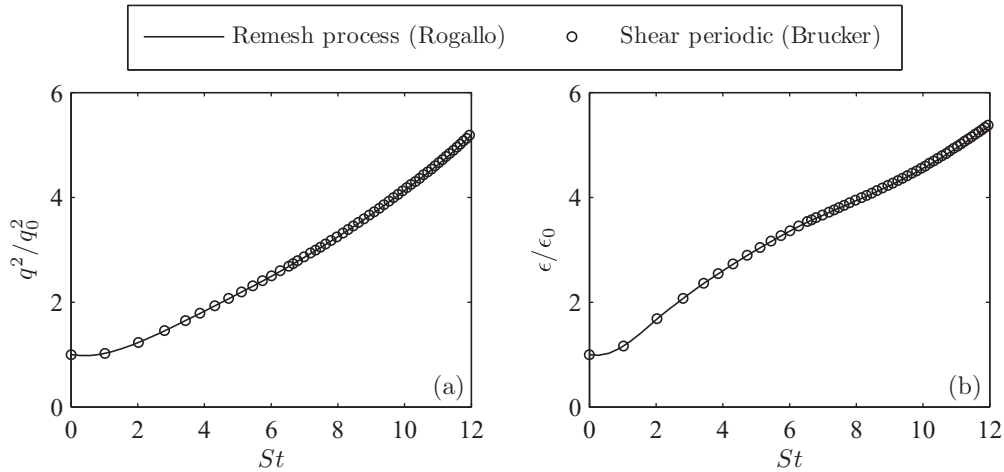


FIG. 17. Comparison of time evolutions of (a) the normalized turbulent kinetic energy  $q^2/q_0^2$ , and (b) the normalized energy dissipation rate  $\epsilon/\epsilon_0$ , obtained with remeshing process (Rogallo) and shear periodic method (Brucker *et al.* [33]), for the test case  $d = 2.7$ .

of this triadic energy exchange significantly reduces at the lower flow field Fourier dimensions. Second, the contribution of the nonlocal triads to the turbulent kinetic energy exchange becomes more pronounced as the flow field Fourier dimension increases.

In connection with the original problem ( $d = 3$ ), the fractally decimated homogeneous turbulent shear flow might be considered as an appropriate framework for investigating different theoretical issues. It is well known that at relatively large periods of time, dynamics of the HTSF large scales approach a self-similar state. Reducing the Fourier dimension increases the temporal window over which the simulations can retain good resolution of the large and small scales. Therefore, the decimated HTSF is a good candidate for investigating this asymptotic state.

The other important feature of the HTSF is the large-scale anisotropy, which appears as the rodlike structures at relatively large shear parameter. These structures are the primary contributor in dynamics of the sublayer of wall-bounded turbulent shear flows. Since by reduction of the Fourier dimension the large-scale anisotropy increases, decimated HSTF can provide a more suitable framework for investigating these vortical structures and their transport mechanism.

Finally, the dynamical coupling between the large and small scales through the nonlocal triadic energy transfer can be controlled by changing the Fourier dimension. At a reduced Fourier dimension, it is possible to isolate the dynamics of the small scales from that of the large scales. Therefore, using

Fourier decimation, it might be possible to investigate the universal state of the small scale of the homogeneous shear flow at a moderate Reynolds number.

APPENDIX

In this Appendix, the consistency of the fractal Fourier decimation and the remeshing procedure is examined. To this end, time evolution of the test case with extreme truncation  $d = 2.7$  is simulated using two different approaches: one with remeshing procedure and the other based on the shear periodic boundary condition. In the latter approach, the skeleton of the preselected set of the active Fourier modes and its fractal dimension remains constant during the simulation (Brucker *et al.* [33]).

Figures 17(a) and 17(b) compare time evolutions of the normalized turbulent kinetic energy  $q^2/q_0^2$  and the turbulent kinetic energy dissipation (enstrophy)  $\epsilon/\epsilon_0$ , obtained from these two schemes. An excellent agreement between the results obtained from both methodologies can be observed. This indicates that within the range of the considered parameters, the combined effects of the remeshing procedure and the fractal Fourier decimation do not affect the results. Moreover, as it can be observed, the aliasing-free remeshing procedure does not result in any discontinuities in time evolutions of these statistics at remeshing time  $St = 1, 3, \dots$ . This shows that the total amount of kinetic energy and enstrophy are almost conserved during the remeshing procedure.

[1] A. Tsinober, *An Informal Conceptual Introduction to Turbulence* (Springer, Berlin, Netherlands, 2009).  
 [2] P. A. Davidson, *Turbulence: An Introduction for Scientists and Engineers* (Oxford University Press, New York, 2004).  
 [3] K. G. Wilson and M. E. Fisher, *Phys. Rev. Lett.* **28**, 240 (1972).  
 [4] W. D. McComb, *Renormalization Methods: A Guide For Beginners* (Oxford University Press, New York, 2007).

[5] R. H. Kraichnan, *Phys. Fluids* **10**, 1417 (1967).  
 [6] R. H. Kraichnan, *J. Fluid Mech.* **47**, 525 (1971).  
 [7] P. Tabeling, *Phys. Rep.* **362**, 1 (2002).  
 [8] H. Kellay and W. I. Goldburg, *Rep. Prog. Phys.* **65**, 845 (2002).  
 [9] S. Fox and P. A. Davidson, *J. Fluid Mech.* **659**, 351 (2010).  
 [10] G. Boffetta and R. E. Ecke, *Annu. Rev. Fluid Mech.* **44**, 427 (2012).

- [11] M. Nelkin, *Phys. Rev. A* **11**, 1737 (1975).
- [12] D. Forster, D. R. Nelson, and M. J. Stephen, *Phys. Rev. A* **16**, 732 (1977).
- [13] J. D. Fournier and U. Frisch, *Phys. Rev. A* **17**, 747 (1978).
- [14] V. S. L'vov, A. Pomyalov, and I. Procaccia, *Phys. Rev. Lett.* **89**, 064501 (2002).
- [15] P. Giuliani, M. H. Jensen, and V. Yakhot, *Phys. Rev. E* **65**, 036305 (2002).
- [16] A. Celani, S. Musacchio, and D. Vincenzi, *Phys. Rev. Lett.* **104**, 184506 (2010).
- [17] U. Frisch, A. Pomyalov, I. Procaccia, and S. S. Ray, *Phys. Rev. Lett.* **108**, 074501 (2012).
- [18] A. S. Lanotte, R. Benzi, S. K. Malapaka, F. Toschi, and L. Biferale, *Phys. Rev. Lett.* **115**, 264502 (2015).
- [19] A. S. Lanotte, S. K. Malapaka, and L. Biferale, *Eur. Phys. J. E* **39**, 49 (2016).
- [20] M. M. Rogers and P. Moin, *J. Fluid Mech.* **176**, 33 (1987).
- [21] M. J. Lee, J. Kim, and P. Moin, *J. Fluid Mech.* **216**, 561 (1990).
- [22] O. Lida, M. Iwatsuki, and Y. Nagano, *Phys. Fluids* **12**, 2895 (2000).
- [23] J. C. Isaza and L. R. Collins, *J. Fluid Mech.* **637**, 213 (2009).
- [24] C. Vanderwel and S. Tavoularis, *J. Fluid Mech.* **754**, 488 (2014).
- [25] H. Tennekes and J. L. Lumley, *A First Course in Turbulence* (MIT Press, Cambridge, MA, 1972).
- [26] J. Mathieu and J. Scott, *An Introduction to Turbulent Flow* (Cambridge University Press, Cambridge, England, 2000).
- [27] R. S. Rogallo, Technical Report No. NASA 81315, 1981.
- [28] D. C. Leslie, *Developments in the Theory of Turbulence* (Oxford University Press, New York, 1973).
- [29] A. Pumir, *Phys. Fluids* **8**, 3112 (1996).
- [30] P. Sagaut and C. Cambon, *Homogeneous Turbulence Dynamics* (Cambridge University Press, Cambridge, England, 2008).
- [31] S. Kida and M. Tanaka, *J. Fluid Mech.* **274**, 43 (1994).
- [32] A. M. Ahmed and S. Elghobashi, *Phys. Fluids* **13**, 3346 (2001).
- [33] K. A. Brucker, J. C. Isaza, T. Vaithianathan, and L. R. Collins, *J. Comput. Phys.* **225**, 20 (2007).
- [34] U. Frisch, *Turbulence: The Legacy of A. N. Kolmogorov* (Cambridge University Press, Cambridge, England, 1995).
- [35] T. Gerz, U. Schumann, and S. E. Elghobashi, *J. Fluid Mech.* **200**, 563 (1989).
- [36] J. A. Domaradzki and R. S. Rogallo, *Phys. Fluids* **2**, 413 (1990).
- [37] A. K. Kuczaj, B. J. Geurts, and W. D. McComb, *Phys. Rev. E* **74**, 016306 (2006).
- [38] K. Okhitani and S. Kida, *Phys. Fluids* **4**, 794 (1992).
- [39] T. Watanabe and T. Iwayama, *Phys. Rev. E* **76**, 046303 (2007).
- [40] M. Buzzicotti, B. P. Murray, L. Biferale, and M. D. Bustamante, *Eur. Phys. J. E* **39**, 34 (2016).
- [41] Y. Zhou, *Phys. Fluids* **5**, 1092 (1993).
- [42] F. Waleffe, *Phys. Fluids A* **4**, 350 (1992).
- [43] J. A. Domaradzki and D. Carati, *Phys. Fluids* **19**, 085112 (2007).
- [44] M. K. Verma, A. Ayyer, O. Debliquy, S. Kumar, and A. V. Chandra, *Pramana* **65**, 297 (2005).
- [45] J. A. Domaradzki and D. Carati, *Phys. Fluids* **19**, 085111 (2007).
- [46] H. Aluie and G. L. Eyink, *Phys. Fluids* **21**, 115108 (2009).